AGU PUBLICATIONS

Water Resources Research

RESEARCH ARTICLE
10.1002/2013WR014864

Special Section:
Patterns in Soil-Vegetation-Atmosphere Systems: Monitoring, Modelling and Data Assimilation

Key Points:
- Multiconfiguration EMI imaging returns quasi 3-D EC variations
- Low-resolution lateral grain size distribution maps confirm lateral EC values
- Formerly obtained ERT transects confirm lateral and vertical EC values

Correspondence to:
C. von Hebel,
c.von.hebel@fz-juelich.de

Citation:
von Hebel, C., S. Rudolph, A. Mester, J. A. Huisman, P. Kumbhar, H. Vereecken, and J. van der Kruk (2014), Three-dimensional imaging of subsurface structural patterns using quantitative large-scale multiconfiguration electromagnetic induction data, *Water Resour. Res.*, *50*, 2732–2748, doi:10.1002/2013WR014864.

Received 9 OCT 2013
Accepted 4 MAR 2014
Accepted article online 6 MAR 2014
Published online 28 MAR 2014

Three-dimensional imaging of subsurface structural patterns using quantitative large-scale multiconfiguration electromagnetic induction data

Christian von Hebel[1], Sebastian Rudolph[1], Achim Mester[2], Johan A. Huisman[1], Pramod Kumbhar[1], Harry Vereecken[1], and Jan van der Kruk[1]

[1]Agrosphere (IBG-3), Forschungszentrum Jülich GmbH, Jülich, Germany, [2]Electronic Systems (ZEA-2), Forschungszentrum Jülich GmbH, Jülich, Germany

Abstract Electromagnetic induction (EMI) systems measure the soil apparent electrical conductivity (ECa), which is related to the soil water content, texture, and salinity changes. Large-scale EMI measurements often show relevant areal ECa patterns, but only few researchers have attempted to resolve vertical changes in electrical conductivity that in principle can be obtained using multiconfiguration EMI devices. In this work, we show that EMI measurements can be used to determine the lateral and vertical distribution of the electrical conductivity at the field scale and beyond. Processed ECa data for six coil configurations measured at the Selhausen (Germany) test site were calibrated using inverted electrical resistivity tomography (ERT) data from a short transect with a high ECa range, and regridded using a nearest neighbor interpolation. The quantitative ECa data at each grid node were inverted using a novel three-layer inversion that uses the shuffled complex evolution (SCE) optimization and a Maxwell-based electromagnetic forward model. The obtained 1-D results were stitched together to form a 3-D subsurface electrical conductivity model that showed smoothly varying electrical conductivities and layer thicknesses, indicating the stability of the inversion. The obtained electrical conductivity distributions were validated with low-resolution grain size distribution maps and two 120 m long ERT transects that confirmed the obtained lateral and vertical large-scale electrical conductivity patterns. Observed differences in the EMI and ERT inversion results were attributed to differences in soil water content between acquisition days. These findings indicate that EMI inversions can be used to infer hydrologically active layers.

1. Introduction

Soil moisture determines the water and energy exchange between the subsurface and the atmosphere. Because of its highly dynamic nature, soil water content in the vadose zone plays an important role in the interaction between the pedosphere, atmosphere, and biosphere [*Vereecken et al*., 2008]. The most commonly used methods to monitor soil water content include gravimetric soil sampling, time domain reflectometry, and capacitance sensors [*Robinson et al*., 2003]. However, these methods only provide point-scale information with a sparse depth resolution and are laborious when covering large areas. Although these limitations have recently been addressed with the introduction of wireless sensor networks [*Bogena et al*., 2010; *Rosenbaum et al*., 2012], the large amount of soil water content sensors required for such a sensor network may be prohibitive from a cost perspective. Large-scale low-resolution soil water content of the upper few centimeters can be derived from air-borne or space-borne remote sensing techniques [*Kerr et al*., 2001; *Montzka et al*., 2011]. Hydrogeophysical measurements have been proposed to fill the gap between point-scale and remote sensing methods and to provide soil water contents with a high lateral and vertical resolution indispensable for catchment-scale hydrological studies [*Robinson et al*., 2008].

Since the required characterization of areas up to the km^2-scale is best performed with contactless and mobile measurement systems, electromagnetic (EM) measurements show a particularly large potential as they respond to soil water content and other soil characteristics, such as soil porosity and soil texture. To characterize aquifers up to several hundred meters depth, helicopter-based time-domain EM methods have been successfully used [*Sørense and Auken*, 2004]. For shallow investigations up to 6 m depth, frequency domain electromagnetic induction (EMI) instruments are more appropriate because the entire system of

©2014. American Geophysical Union. All Rights Reserved.

transmitter and receiver units can be carried in one mobile construction with fixed coil separations up to 4.0 m. Several researchers have used EMI to determine soil water content or to study hydrological processes. For example, soil water content was successfully related to bulk soil electrical conductivity by *Sheets and Hendrickx* [1995], soil strata were determined using EMI by *Corwin and Lesch* [2005] and *Sudduth et al.* [2005], and the influence of the water content and salinity on the measured signal has been investigated by *Hardie and Doyle* [2012]. At a larger scale, *Abdu et al.* [2008] inferred soil texture and water holding capacity from EMI measurements. In a further study, *Robinson et al.* [2009] imaged soil water dynamics using repeated measurements performed with an EMI system over a period of several months. They tried to tease apart the contributions of time-invariant soil properties (e.g., clay content) and the dynamic contributions of soil water content and the electrical conductivity of the soil solution to the observed apparent electrical conductivity (ECa). Zones of water depletion and accumulation were identified, such that the obtained ECa maps showed different states of soil moisture and provided qualitative insights in hydrological patterns and pathways. Hence, EMI surveys were found to be useful when determining soil spatial variability in the watershed [*Robinson et al.*, 2012].

In most studies, EMI measurements are performed with a single source-receiver system to qualitatively map the spatial ECa patterns and to subsequently relate them to the soil properties and/or water content. Recently, a new generation of multiconfiguration EMI systems has become commercially available. These systems consist of one electromagnetic field transmitter and various receivers with different coil separations and coil orientations [*Saey et al.*, 2012; *Santos et al.*, 2010]. Such systems enable the simultaneous sensing over different depth ranges, since the measured ECa is a weighted average over a specific sensing depth that depends on both coil separation and coil orientation [*Kaufman and Keller*, 1983]. In principle, these multiconfiguration data can be used to invert for electrical conductivity changes with depth because the measured ECa values reflect different but overlapping soil volumes. A prerequisite for reliable inversions is that the measured ECa values are accurate and precise. However, external influences such as the presence of the operator, zero-leveling procedures, cables close to the system and/or the field setup used to move the sensors can significantly affect the precision of the measurements [*Gebbers et al.*, 2009; *Nüsch et al.*, 2010; *Sudduth et al.*, 2001]. Therefore, the EMI data sets need to be calibrated to obtain quantitative apparent electrical conductivities.

One option to calibrate ECa measured with EMI uses soil cores as ground truth data. This approach was successfully applied by *Triantafilis et al.* [2000] and *Moghadas et al.* [2012]. They recorded ECa at sampling locations and calibrated those against the theoretical EMI response calculated from the true electrical conductivity distribution measured at regular depth increments of particular soil cores. However, drilling at numerous sampling locations may be required. Another calibration approach relies on a linear regression between predicted apparent electrical conductivities obtained from a Maxwell-based full-solution EM forward model using inverted ERT data as input and the ECa values recorded with EMI along the same transect [*Lavoué et al.*, 2010; *Minsley et al.*, 2012].

Sudduth et al. [2013] inverted calibrated EMI data for two-layer and three-layer subsurface models using the linear local sensitivity forward model of *McNeill* [1980] that estimates ECa under the low induction number (LIN) approximation, i.e., the induction number has to be much smaller than unity. However, *Beamish* [2011] restricted this model to environments with very low electrical conductivities ($<$12 mS/m). An alternative inversion approach was introduced by *Mester et al.* [2011]. They inverted calibrated multiconfiguration EMI data to obtain a two-layer subsurface model using a combined global-local search procedure. The global search was performed with the linear local sensitivity forward model, whereas the subsequent local search used a complete EM forward model based on the equations given by *Wait* [1982] and *Anderson* [1979]. Imaging of a two-layered three-dimensional (3-D) subsurface volume using large-scale EMI measurements was performed by [*Saey et al.*, 2012] to discriminate subsoil features, to identify the depth to interface between contrasting materials [*Saey et al.*, 2013] and to develop a 3-D hydraulic conductivity model [*Brosten et al.*, 2011], while using the linear local sensitivity model with limited validity.

In our work, we aim to invert large-scale multiconfiguration EMI data using the Maxwell-based full-solution EM forward model to resolve the 3-D multilayer electrical conductivity structures that are related to different soil constituents. The multiconfiguration ECa data are calibrated following the approach of *Lavoué et al.* [2010], and processed with a novel filter strategy. A novel three-layer inversion scheme is introduced that relies on an efficient parallelized global optimization algorithm and a full-solution horizontally layered EM

© 2014. American Geophysical Union. All Rights Reserved.

forward model. The inversion is tested using a synthetic data set and applied to experimental data acquired over an area of approximately 11,400 m^2. For each grid location, the processed and regridded experimental EMI data are independently inverted and stitched together to form a quasi-3-D image. Horizontal depth slices are compared with grain size distributions and vertical slices are validated with ERT transects.

2. Theoretical Background

2.1. Electromagnetic Induction Theory

Frequency domain electromagnetic induction (EMI) systems use an alternating current with a fixed frequency that passes through a transmitter coil and generates a primary magnetic field. This time-varying primary magnetic field induces eddy currents in a conductive subsurface, which in turn generate a secondary magnetic field. The interference of the primary and the secondary magnetic field is measured at a receiver coil. An increasing quadrature component of the ratio between the secondary and primary magnetic field can be related to an increasing apparent electrical conductivity of the subsurface [*Keller and Frischknecht*, 1966; *Ward and Hohmann*, 1988].

EMI instruments typically have several operational modes or coil configurations. The most commonly used coil configurations are so-called coplanar loops in which both transmitter and receiver coils are either oriented horizontally or vertically with respect to the ground surface. As a rule of thumb, vertical coplanar (VCP) loops sense the ground up to a depth of approximately 0.75 times the coil separation while horizontal coplanar (HCP) loops sense depth levels of approximately 1.5 times the coil offset. However, these sensing depths are only approximate since the electrical conductivity of the ground and the applied frequency also affect the penetration depth. Most natural soils are stratified and often the layers have different electrical conductivities, e.g., due to differences in soil water content, porosity or clay content. When performing EMI measurements over such a layered medium, the measured value represents a nonlinear average of the electrical conductivity of the different layers. The strength of the induced secondary magnetic field depends on the electrical properties of the specific layers and can be modeled most accurately using an exact EM forward model, which is described in the following section.

2.2. Forward Modeling of a Multilayered Earth

An EM forward model uses the electrical conductivity σ and corresponding layer thickness h to predict the magnetic field H. More general, $\mathbf{H} = \mathrm{FM}(\mathbf{p})$, where **H** are the predicted values for a number of source-receiver configurations, FM is the forward model, and **p** are the model parameters (σ_i, h_j), where $i = 1\ldots n$ and $j = 1\ldots n-1$, for an n-layered earth.

The secondary magnetic field measured with an EMI system over a horizontally layered earth in either the VCP or the HCP mode can be described according to *Wait* [1982] as

$$H^{VCP}=1-\ s^2\int_0^\infty R_0 J_1(s\lambda)\lambda d\lambda, \tag{1}$$

$$H^{HCP}=1-\ s^3\int_0^\infty R_0 J_0(s\lambda)\lambda^2 d\lambda \tag{2}$$

where J_0 and J_1 are the Bessel functions of zero and first order, respectively, and R_0 is the reflection coefficient [*Ward and Hohmann*, 1988]

$$R_n=\frac{\frac{\Gamma_n-\Gamma_{n+1}}{\Gamma_n+\Gamma_{n+1}}+R_{n+1}\exp\left(-2\Gamma_{n+1}h_{n+1}\right)}{1+\frac{\Gamma_n-\Gamma_{n+1}}{\Gamma_n+\Gamma_{n+1}}R_{n+1}exp\left(-2\Gamma_{n+1}h_{n+1}\right)}, \tag{3}$$

where $\Gamma_n=\ \sqrt{\lambda^2+\gamma_n^2}$, λ^2 is the radial wavenumber, $\gamma_n^2=\ \sqrt{j\omega\mu_0\sigma_n}$ is the propagation constant of low-frequency electromagnetic fields, $j^2 = -1$ is the imaginary unit, ω is the angular frequency, μ_0 is the magnetic susceptibility (of free space), and σ_n is the electrical conductivity of the n-th layer. The reflection

© 2014. American Geophysical Union. All Rights Reserved.

coefficient can be obtained in a recursive manner, which is initiated by the observation that there are no upcoming waves from the lower half space, so $R_{n+1} = 0$ [*Slob and Fokkema*, 2002]. This electromagnetic forward model is considered exact because it uses only the low-frequency ($<10^5$ Hz) approximation, which assumes that the EM field only propagates due to conduction currents. It includes the angle-dependent reflection coefficients between the different layers and their pertaining layer thicknesses [*Lavoué et al.*, 2010]. Moreover, the height of the instrument above ground can in principle be included, which would allow the signal strength of off-ground electromagnetic induction systems to be predicted.

2.3. Low Induction Number Local Sensitivity Model

From the described equations, the sensitivities for the different coil configurations are not directly evident. A simple estimation of the earth response for a low-frequency electromagnetic excitation is given by the local sensitivities [*McNeill*, 1980]. These local sensitivities are derived using the LIN approximation and describe the total secondary magnetic field as the sum of independent contributions generated within individual subsurface layers at different depth levels. Figure 1 shows local sensitivity curves for the VCP and HCP modes with three different coil separations, i.e., $s = 0.32$ m, $s = 0.71$ m, and $s = 1.18$ m. These coil configurations are presented because they were used to acquire the experimental data shown later.

It can be seen that the VCP mode displayed in Figures 1a and 1b are most sensitive to near-surface layers and less sensitive to deeper layers, i.e., the contribution to the secondary magnetic field decreases relatively fast with increasing depth. The HCP sensitivities shown in Figures 1c and 1d are less sensitive to the shallow layers, but peak at increased depths that depend on the coil separation. Consequently, the sensitivities for the different coil separations in Figure 1 demonstrate that the main contributions to the secondary magnetic field for the different EMI coil configurations originate from different depth levels. Thus, measurements with different coil configurations can be used to infer multilayered electrical conductivity models of the subsurface [*McNeill*, 1980].

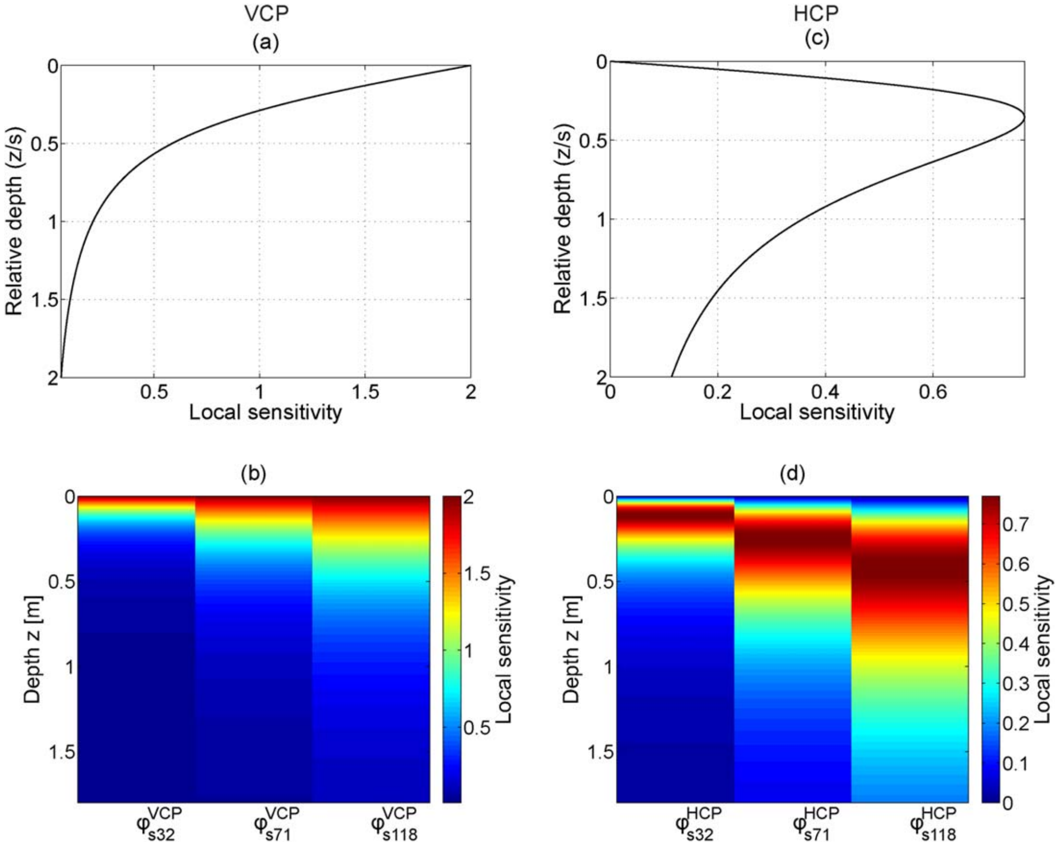

Figure 1. Local sensitivity functions for depth normalized to coil separation for (a) VCP and (c) HCP. (b and d) Corresponding depth sensitivities for different EMI coil separations s in centimeter (after *McNeill* [1980]).

© 2014. American Geophysical Union. All Rights Reserved.

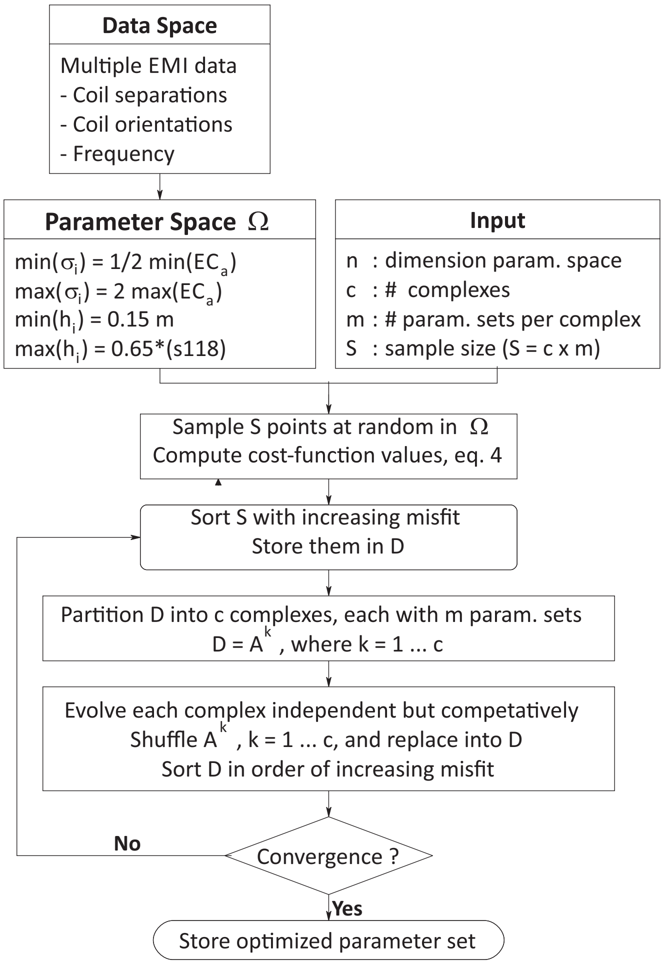

Figure 2. Flowchart of the SCE inversion algorithm (after *Duan et al.* [1992]).

2.4. MultiConfiguration EMI Inversion Algorithm

To reconstruct the electrical conductivity structures from EMI data, we introduce an inverse modeling scheme that optimizes the normalized L_1-norm using the following objective function, also called cost or misfit function,

$$\Delta \mathrm{H}(\mathbf{p})=\frac{1}{M}\sum_{m=1}^{M}\frac{\left|\mathrm{H}_{\mathrm{m}}^{\mathrm{mea}}-\mathrm{H}_{\mathrm{m}}^{\mathrm{mod}}(\mathbf{p})\right|}{\left|\mathrm{H}_{\mathrm{m}}^{\mathrm{mea}}\right|}, \tag{4}$$

where ΔH describes the misfit between the measured magnetic field, $\mathrm{H}_{\mathrm{m}}^{\mathrm{meas}}$, and the modeled magnetic field, $\mathrm{H}_{\mathrm{m}}^{\mathrm{mod}}$, and M is the number of coil configurations including different separations and orientations. The absolute difference norm (L_1-norm) is used because it is less influenced by outliers compared to the more traditional squared difference norm (L_2-norm). Moreover, no smoothing or damping parameters were considered to assure sharp layer boundaries between adjacent structures.

This objective function was already successfully used by *Mester et al.* [2011], who implemented a combined global-local search that used the local sensitivity and the exact EM forward model, respectively, to invert for two layers described by two electrical conductivity values (σ_i, i = 1,2) and one layer thickness (h_j, j = 1). A straightforward extension of their two-layer inversion approach for three layers (σ_i, i = 1,2,3, and h_j, j = 1,2) was not successful due to the higher dimensionality of the parameter space, which resulted in the inversion being trapped in local minima, possibly also due to the use of the LIN approximation in the global search. Consideration of lateral constraints for neighboring inversions similar to *Auken et al.* [2005] resulted in a directional dependency, which also indicated that the obtained inversion results were not optimal and most likely affected by improper convergence of the global-local search to local minima.

For an improved exploration of the user-defined parameter space, we parallelized the shuffled complex evolution (SCE) algorithm. The SCE is a global optimization that combines deterministic strategies to guide the search with the inclusion of random elements that help to make the algorithm flexible and robust [*Duan et al.*, 1992]. Here, a population spread out over the feasible parameter space is divided into subpopulations, called complexes, where each complex carries information on number, location and size of the major regions of attraction [*Mboh et al.*, 2011; *Vrugt et al.*, 2003]. The implementation of an implicit clustering strategy helps to concentrate the search in the most promising regions [*Duan et al.*, 1992].

The minimum and maximum values of the parameter space explored by the SCE algorithm were determined as follows. For the electrical conductivity of each layer, the minimum and maximum values were determined by multiplying the smallest ECa by 0.5 and by doubling the largest ECa to ensure that the parameter space covers a wide range of possible electrical conductivity values. The minimum value for the layer thickness was

© 2014. American Geophysical Union. All Rights Reserved.

0.15 m due to the used numerical integration approach as described in *Mester et al*. [2011] and the maximum layer thicknesses were set to 0.35 and 0.76 m for the first and second layer, respectively. In agricultural fields these minimum and maximum values are appropriate to describe the ploughing layer, while the maximum thickness of the second layer is related to the maximum contribution to the secondary magnetic field of the deepest sensing coil configuration (see Figure 1d). Deeper material changes can only be reliably detected when sensors with larger coil separations are also used in EMI data acquisition.

The SCE algorithm starts by randomly sampling S = c x m initial parameter sets from the five-dimensional space (Figure 2), where tests indicated that the use of c = 5 complexes and m = 11 members in a complex resulted in reliable inversion results. The objective function is evaluated for each parameter combination, after which the parameter sets are sorted with increasing misfit into an array D, that is partitioned into A^k, k = 1. . .c, complexes. A systematic strategy evolves each complex independently, according to the competitive complex evolution (CCE) algorithm, i.e., in each complex the space is searched in different directions while a triangular probability distribution ensures competitiveness [*Duan et al*., 1993]. Then the evaluated complexes A^k, k = 1. . .c, are shuffled and replaced into matrix D, where the parameter sets are sorted again with increasing misfit. The evolution and shuffling processes are continued until one of the two following convergence criteria has been reached: (1) maximum of 5000 function evaluations or (2) improvement smaller than 0.01% within 10 CCE loops. The competitive complex evolution and shuffling process in the SCE algorithm enhances survivability and improves global convergence efficiency, since better parameter sets are preferred over worse ones [*Duan et al*., 1993; *Mboh et al*., 2011]. Note that the implemented SCE optimization inverts the large-scale multiconfiguration EMI data of each measurement position separately, i.e., assuming a 1-D layered model. Due to numerous inversions, the parallelized SCE algorithm runs on the JUROPA—supercomputer of Forschungszentrum Jülich using GNU Octave, Version 3.4.3.

To test the reliability of the inversion scheme, we first generated synthetic noise-free and noise-contaminated EMI data for three different 1-D models using equations (1) and (2). Here, the electrical properties of the selected homogeneous model, two-layer model and three-layer model (red lines in Figure 3) coincide with the test site structures as described later.

Figures 3a–3c shows the inversion result for noise-free data. The implemented three-layer SCE inversion reconstructed the models without deviations except for the three-layer case, where the electrical conductivity of the second layer deviated by 0.2 mS/m. This small difference was considered to be

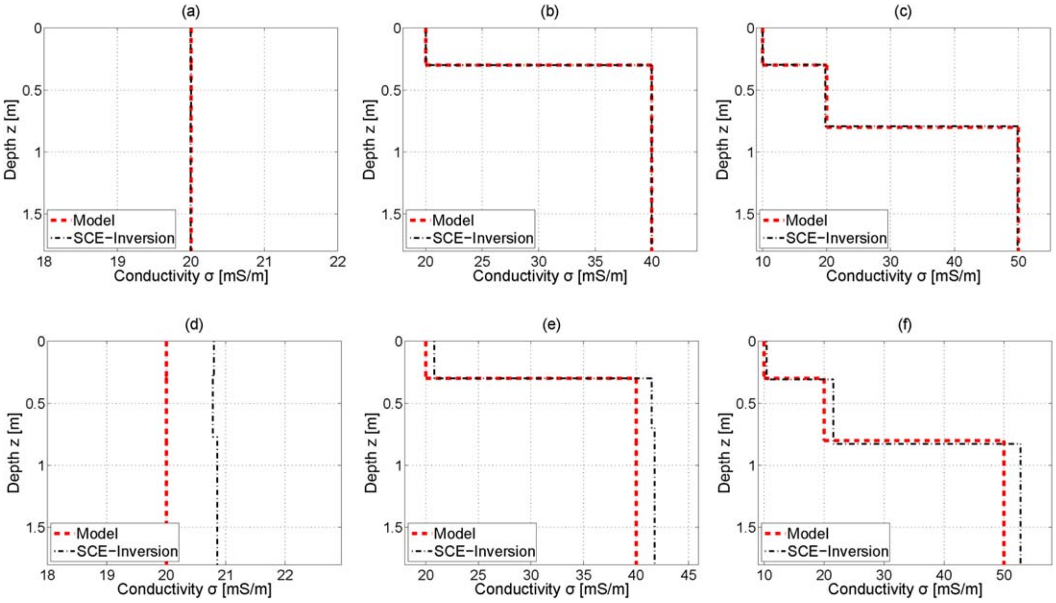

Figure 3. (a–c, top) Model inversion of synthetic data without noise and (d–f, bottom) with 4% coil specific ECa added as noise to the data. (a and d) Homogeneous model, (b and e) Two-layer model, and (c and f) Three-layer model (dashed red line). The dashed black line shows the inversion result obtained with the shuffled-complex-evolution (SCE) optimization implemented for three layers.

negligible and has not been further investigated. The inversion results of the noise-contaminated data are shown in Figures 3d–3f. Due to the instruments accuracy (detailed later), we added 4% of the generated coil specific ECa to the data. The reconstruction of the homogeneous model deviated by 0.8 mS/m (Figure 3d) from the input model. For the two-layer case shown in Figure 3e, the three-layer SCE inversion found 20.8 mS/m and 0.3 m thickness for the first layer and reconstructed the lower half-space with 41.5 and 41.8 mS/m. Figure 3f shows the inverted parameters for the three-layer model. The electrical conductivity of the first layer slightly deviated from the input model, while the inverted electrical conductivity of the second layer and lowest zone deviated more strongly with about 1.5 and 2.5 mS/m, respectively. The estimated depth of the first and second layer boundaries deviated by only 1 and 2 cm, respectively. Evidently, the implemented SCE inversion reconstructs the presented cases reasonably well using both noise-free and noisy data indicating its applicability to experimental EMI data.

3. Materials and Methods

3.1. Study Area

The Selhausen test site has a size of about 190 m in east-west and about 60 m in north-south direction and is situated in the southern part of the Lower Rhine Embayment in Germany. The underlying sediments are Quarternary sediments, which are mostly fluvial deposits from the Rhine/Meuse and Rur river system covered by floodplain sediments from the Pleistocene and Holocene. Generally, the topsoil water content is lower in the eastern than in the western part of the test site and the groundwater table fluctuates seasonally but is typically below 3 m depth [*Weihermüller et al.*, 2007].

The soil type of the test site was described as silty loam according to the USDA textural classification with a distinct gradient in soil texture (coarse to fine) from east to west. Figure 4 shows the grain size distribution of the upper 0.3 m sampled at a 10 by 10 m soil sampling grid. The eastern part of the test site is mainly composed of coarse material (>2 mm) with a mass fraction up to 50% and a considerable amount of sand. Toward the west, the silt and clay content increase up to 69 and 18%, respectively.

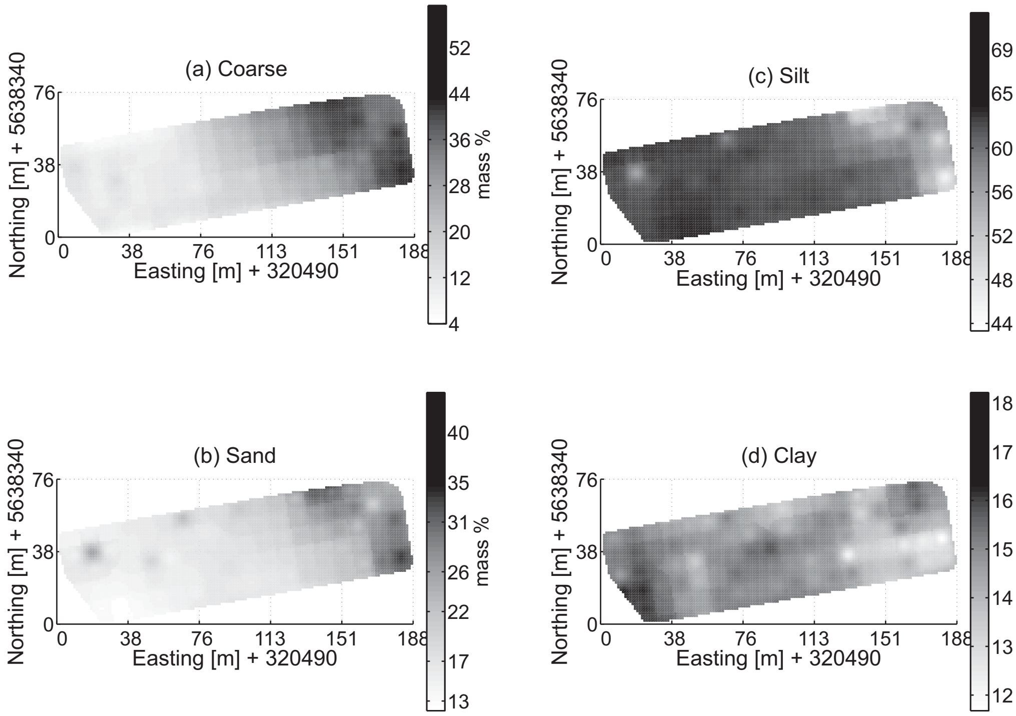

Figure 4. Grain size distribution for a 10 by 10 m coarse grid of the upper 30 cm depth at the Selhausen test site. (a) Coarse fraction, (b) Sand, (c) Silt, and (d) Clay. The distribution shows a higher gravel content in the eastern part and variably distributed sand, silt, and clay-rich areas toward the west.

© 2014. American Geophysical Union. All Rights Reserved.

3.2. EMI and ERT Data Acquisition

EMI measurements were carried out at the Selhausen test site on 29 June 2012 using the CMD-MiniExplorer (GF-Instruments, Brno, Czech Republic). This system uses one electromagnetic field transmitter and three receiving coils with different separations and can be oriented in VCP or HCP mode. The offsets between transmitter and receivers are 0.32, 0.71, and 1.18 m referred hereafter as s32, s71, and s118. The sensors have an accuracy of 4% (at 50 mS/m) and are factory calibrated [*GF-Instruments*, 2011] such that the device requires no zero leveling on site. The EMI sensor was acclimated to outside temperature using a 30 min warm-up time and then pulled on a wooden sled behind an all-terrain-vehicle (ATV) at approximately 6–8 km/h. Measurements were carried out with a sampling rate of 10 Hz, hence ECa data were measured every 16–18 cm. Over the whole survey area, first east-western tracks with about 3 m distance and thereafter perpendicular tracks with about 13 m distance were continuously recorded. Very similar ECa values were measured at the intersection of these lines, which indicates that no time drift occurred in the data. In total, six high-resolution data sets of approximately 55,000 measurements were recorded using VCP and HCP modes and three coil separations. The total acquisition time was 3 h. The continuous measurements were georeferenced with a single frequency global positioning system (GPS) using the standard positioning service.

To calibrate the EMI data, a suitable 30 m transect with strong lateral variations of soil apparent electrical conductivity (referred to as the 2012 transect in the following) was identified in the large-scale EMI measurements. On this transect, we consecutively acquired EMI and ERT data. The EMI data were measured stepwise every 0.5 m with the sensor mounted on the sled. ERT measurements were carried out using 120 electrodes with an electrode spacing of 0.25 m using the Syscal Pro system (IRIS Instruments, Orleans, France) and a Dipole-Dipole electrode array. This electrode array was selected because it was found to be most useful to measure resistivity changes in the lateral direction [*Kirsch*, 2009], and to resolve electrical conductivity changes in the shallow subsurface. The data set contained 6715 measurements at various depth levels down to 3.4 m and the acquisition time for the ERT measurements was 3 h, including installation, data acquisition, and removal of electrodes and cables.

On 28 May 2009 and 21 October 2010, 120 m long ERT transects were measured using a roll-along procedure with 15 m overlap at two different locations at the test site by *Lavoué et al*. [2010] and *Busch et al*. [2014]. Whereas the 2012 transect was used for calibration and as a reference for the EMI inversion, the two transects from 2009 and 2010 were used as an independent validation of the quasi 3-D EMI-inversion results.

3.3. Processing and Filtering

The recorded ERT data were filtered using the automatic filtering and deviation filter, set to 2.5%, provided by Prosys II (IRIS Instruments, Orleans, France). The subsequent data set was inverted using Res2DInv (Geotomo Software Sdn. Bhd., Penang, Malaysia). A robust inversion scheme with the default damping parameters was used, which is more suitable for homogeneous regions with sharp boundaries than the default least-square inversion [*Loke et al.*, 2003]. It uses the L_1-norm and tends to produce models that are locally constant within connected regions.

Since our EMI three-layer inversion algorithm assumes a horizontally layered earth, we implemented filter strategies to remove EMI data measured at locations where strong lateral heterogeneity is present. The 2012 transect (calibration line) EMI data were processed by excluding values larger and smaller than the median plus/minus two times the median absolute deviation. The excluded values were replaced using linear interpolation between neighboring values. To flatten peaks in the data, a five point (or 2.5 m) simple moving average was applied.

Large-scale EMI data are rarely normally distributed [*Minsley et al.*, 2012], although this is required for most filter strategies. To overcome this limitation, we developed a novel histogram-filter that identifies and excludes outliers. The histogram filter bins the EMI data into 15 equally spaced containers and computes the percentage of the data within each container. A bin containing $<$0.5% of the data is considered to carry outliers and is thus removed. This filter strategy effectively removes outliers without assuming a normal distribution. In addition, we exclude strongly laterally varying ECa values, where the deviation exceeds 1 mS/m between the actual measurement and adjacent recordings. Finally, the filtered data were smoothed with a 10 point moving average, i.e., over one 10 Hz sampling term. Due to the applied filters, the six multiconfiguration EMI data sets were unequally long. Therefore, the data were regridded using a nearest neighbor interpolation with a grid size of 1.25 m in both spatial directions.

© 2014. American Geophysical Union. All Rights Reserved.

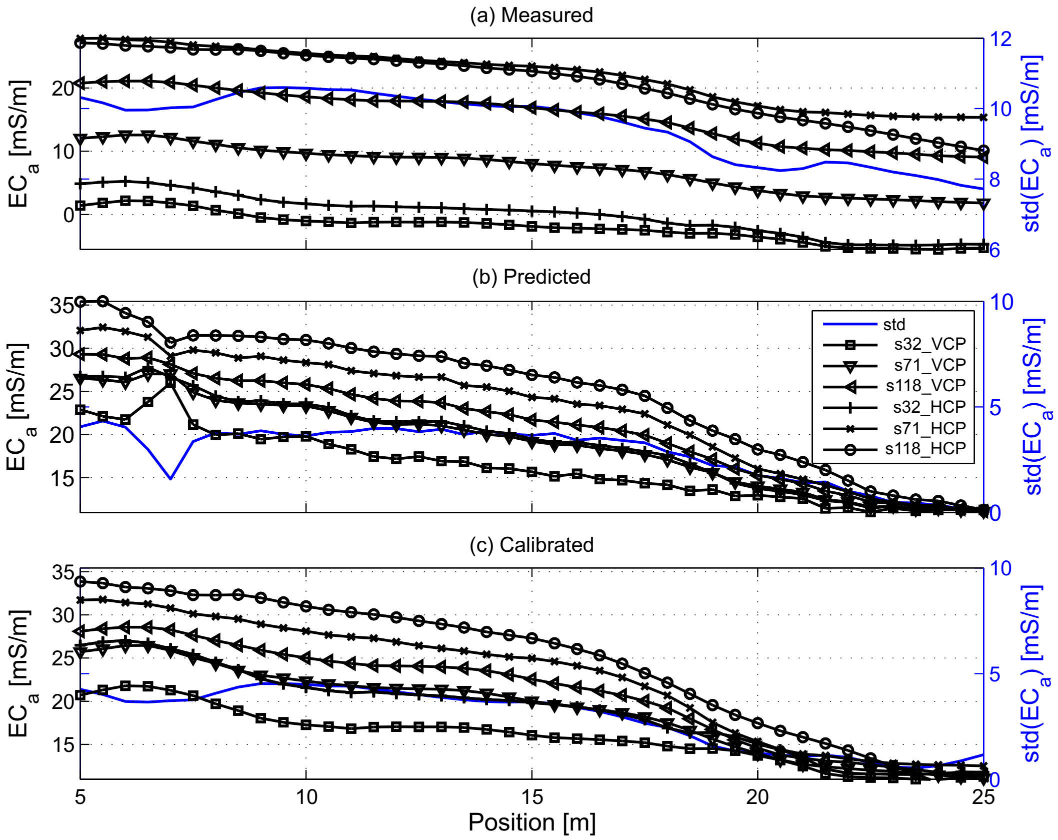

Figure 5. (a) Measurements smoothed with a simple moving average over five positions, (b) Predicted data using a Maxwell-based full-solution EM forward model and inverted ERT data as input, and (c) Postcalibrated EMI data using linear regression parameters. Note that Figures 5b and 5c shows a similar ECa range, whereas Figure 5a shows a similar trend but different scale. The blue lines are the standard deviations at each position, where a small deviation indicates more uniform soil conditions.

4. Results and Discussion

4.1. Calibration and Inversion of the Data Along the Calibration Line

The EMI data measured along the 2012 transect that was identified in the large-scale measurements is presented in Figure 5a. Here the six coil configurations (three coil offsets for VCP and HCP modes) showed increasing ECa values with increasing sensing depth ranging from approximately 1 mS/m for the very shallow sensing VCP coil to about 25 mS/m for the deepest sensing HCP coil at the beginning of the transect. Toward the end of the calibration line, a decreasing trend with a drop of about 5–10 mS/m was observed for all coil configurations, indicating a structural change along the 2012 transect. Note that even negative values were measured pointing toward the need for calibration.

The collocated ERT measurement showed a high repeatability, since the mean quality factor of the raw data was 0.33% and the standard deviation 2.53%. The applied filtering discarded 1.44% (97 out of 6715) of the data. The subsequent data set was inverted and the absolute error was 1.6% after five iterations. This indicates that the ERT data were described well by the inverted subsurface electrical conductivity model (Figure 6b). Note that the first and last 5 m of the ERT transect are not presented because the inversion results are less reliable here. Moreover, the depth range of the presented ERT inversion result is reduced to match the maximum EMI sensing depth (Figure 6a).

To indicate the EMI sensing volume, the definition of *McNeill* [1980] is used for the vertical dimension, whereas the sensing radius of *Callegary et al.* [2012] was considered for the lateral dimension, i.e., approximately 1.5 times the coil separation. A comparison of EMI sensing volumes (Figure 6a) with the corresponding ERT sensing volumes (∼electrode distance divided by 2, Figure 6b) clearly shows that for small and large electrode distances the EMI sensing volume is larger or smaller, respectively. To avoid that inverted

©2014. American Geophysical Union. All Rights Reserved.

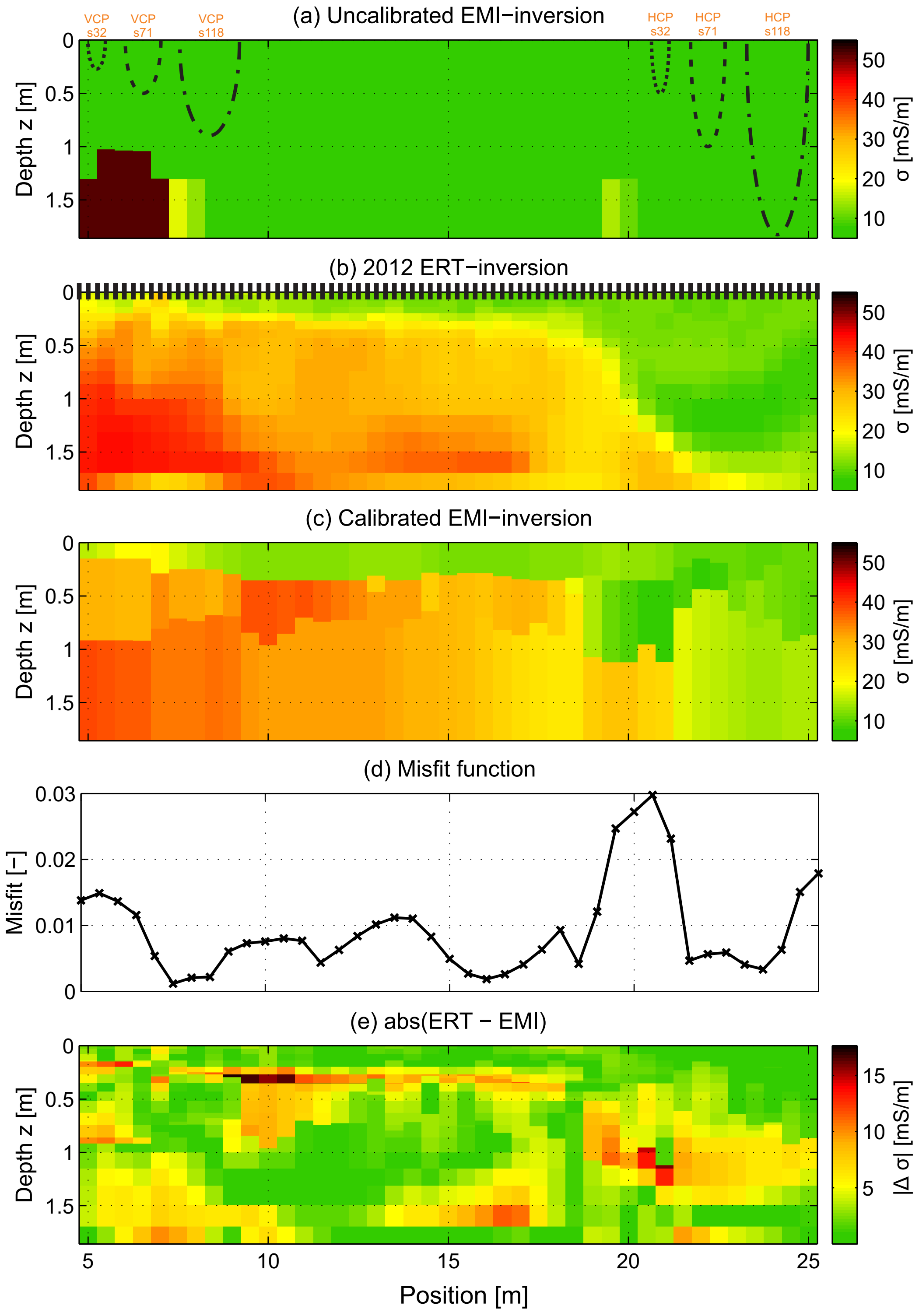

Figure 6. (a) Uncalibrated EMI data inversion result and CMD sensor with sensing depth for s32, s71, and s118 for VCP (left) and HCP (right), (b) ERT reference and calibration model and electrode setup with 0.25 m spacing, (c) calibrated EMI data inversion result, (d) corresponding misfit plot, and (e) absolute difference between the ERT and EMI model.

ERT images are overly smoothed in the lateral direction (i.e., more than the maximum lateral EMI sensing dimension of about 2 m), we used small Dipole-Dipole arrays with a small electrode spacing and a robust inversion approach, as was previously used by *Lavoué et al.* [2010] and *Mester et al.* [2011]. We found that

© 2014. American Geophysical Union. All Rights Reserved.

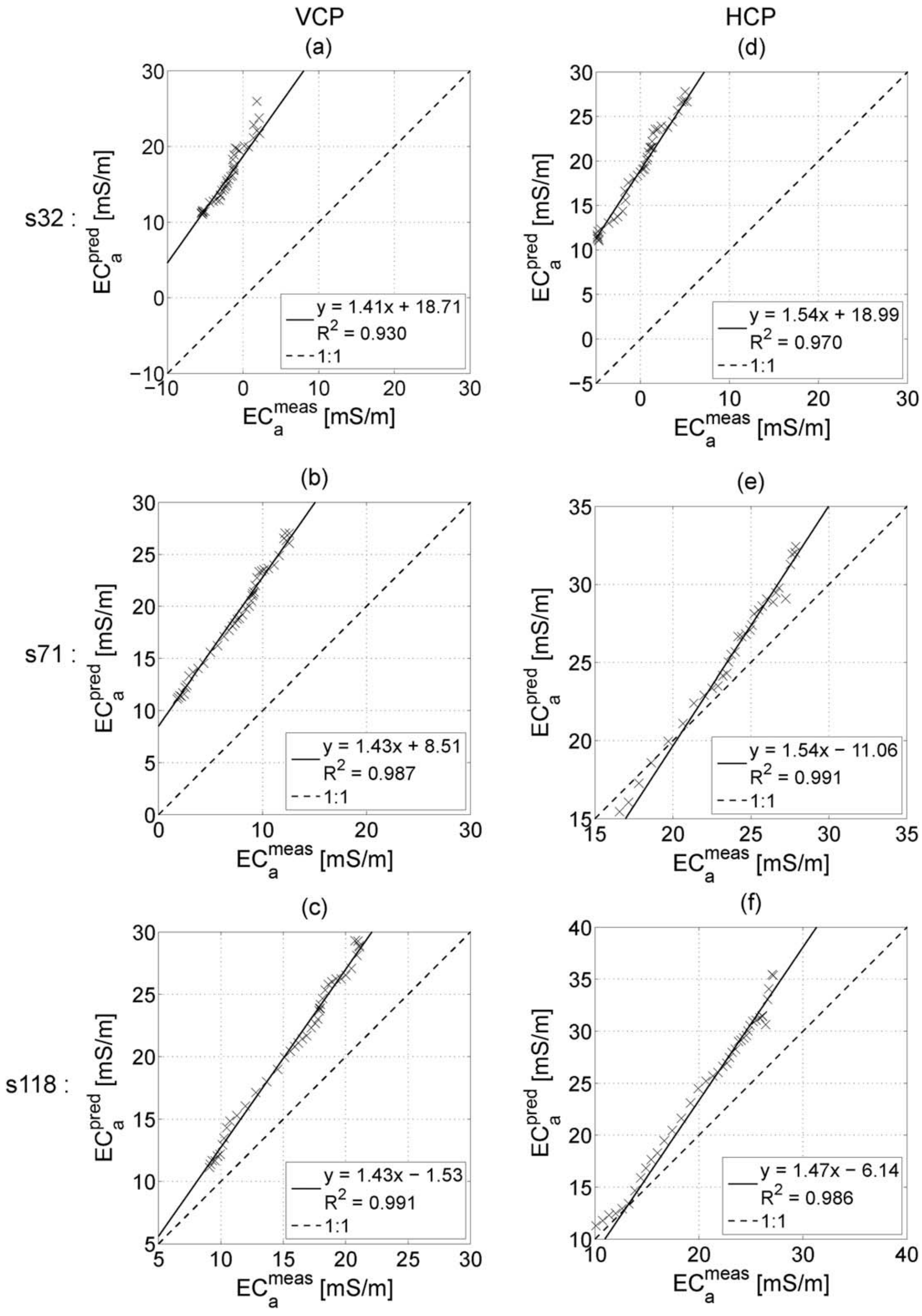

Figure 7. (a, c, and e) Regression plots for measured and predicted data of each coil separation for VCP. (b, d, and f) The HCP mode. Two coil specific regression parameters (scale and shift) calibrate the data, indicated in the legends. Note the coefficients of determination (R^2).

this inversion approach results in piecewise constant electrical conductivity areas that approximately match the size of the EMI sensing volume. Nevertheless, future work should explore which ERT acquisition strategies are best suited for EMI calibration.

© 2014. American Geophysical Union. All Rights Reserved.

Table 1. Mean Absolute Deviation (MAD) Between Calibrated and Uncalibrated Data Shown in Figures 5a and 5c

Coil Separation	VCP (mS/m)	HCP (mS/m)
MAD (Calibrated, Uncalibrated)		
s32	19.0	17.9
s71	2.3	11.6
s118	3.8	5.1

Inversion results for uncalibrated EMI data are presented in Figure 6a. Evidently, this inversion result does not match the electrical conductivity distribution obtained by the ERT inversion results shown in Figure 6b. Next, we calibrated the EMI data using the inverted ERT data as input in equations (1) and (2) to predict apparent electrical conductivities along the calibration line. Compared to the measured EMI data, the predicted ECa curves shown in Figure 5b have similar shapes but different absolute values. To investigate the difference between the measured and predicted ECa values in more detail, these ECa values are plotted against each other in Figure 7. The left column shows the VCP mode while the right column shows the HCP mode with increasing coil separation, s32, s71, and s118, from top to bottom. The predicted data have mostly larger ECa values compared to the measured data such that a clear deviation from the 1:1 line is observed. Hence, the measured EMI data were biased and not suitable for inversion (as shown in Figure 6a). To remove the bias, we performed a linear regression between measured and predicted ECa for each coil configuration, which returned R^2 values larger than 0.93 in all cases (see Figure 7). The obtained regression parameters (scale and shift) are provided in the legends of Figure 7 and indicate that each coil configuration requires a specific calibration to remove the bias from the measured EMI data. To investigate the bias, Table 1 shows the mean absolute deviation (MAD) between the uncalibrated and calibrated data, which was largest for the small coil offsets with values up to 19 mS/m. We judge that these corrections are dominant and that a possible bias due to uncertain ERT inversion results has a minor influence compared to the calibrations that are needed to obtain more reliable ECa values.

Figure 5c shows the calibrated EMI data that are now very similar to the predicted curves presented in Figure 5b. Analyzing the standard deviation of all ECa values as a measure for the variation of the electrical conductivity with depth, relatively small values were observed between 20 and 25 m indicating a more homogeneous subsurface, whereas the larger standard deviation between 5 and 20 m provides a strong indication for a layered subsurface, since the ECa values increase with increasing sensing depth. These homogeneous and layered parts of the calibration transect are also clearly visible in the ERT inversion (Figure 6b), which provides confidence that the calibrated ECa values can now be considered accurate, unbiased, and quantitative.

The calibrated ECa values of the six EMI coil configurations were inverted with the SCE inversion approach for a three-layer medium without regularization. The obtained results are presented in Figure 6c and show smoothly changing electrical conductivity values. Compared to the ERT inversion results, the shallow low-conductivity layer with an electrical conductivity of 10 mS/m was well reconstructed by the EMI inversion in terms of absolute conductivity as well as layer thickness. For the deeper structures, the profile can be divided into three parts. A clear layering was found between 5 and 18 m. The SCE inversion scheme reasonably reconstructed the interface around 0.8 m depth for the first 5–9 m in terms of both layer thickness and electrical conductivity. Instead of an increasing electrical conductivity with depth as can be observed in the ERT data, a high-conductive intermediate layer was obtained by the EMI inversion between 9 and 18 m, which is probably due to a limited sensitivity for the deeper layers of the currently used EMI coil configurations (see also the sensitivity curves in Figure 1). The down-dipping transition zone between 18 and 22 m was approximated with an abrupt change of the electrical conductivity distribution in both lateral and vertical directions, because the inversion algorithm assumes a horizontally layered medium. Note that this region was associated with larger misfits between measured and modeled EMI data (Figure 6d), which indicates that the used model is not entirely appropriate to explain the data. This can only be resolved with a two-dimensional or three-dimensional EMI forward and inverse scheme, which will significantly increase the required computational resources. Between 22 and 25 m, a homogeneous electrical conductivity area was present in the ERT data that was also well reconstructed by the EMI inversion.

Figure 6e shows the absolute difference between the ERT and the calibrated EMI inversion results. Here it can be seen that the EMI inversions were well able to reconstruct the reference model, since almost 90% of the absolute electrical conductivities deviated less than the maximum MAD of 5.8 mS/m. Especially the shallow top layer was well reconstructed, whereas larger differences were present in the deeper subsurface. The largest deviations could be observed at the layer boundaries. On the one hand, this can be caused by the

© 2014. American Geophysical Union. All Rights Reserved.

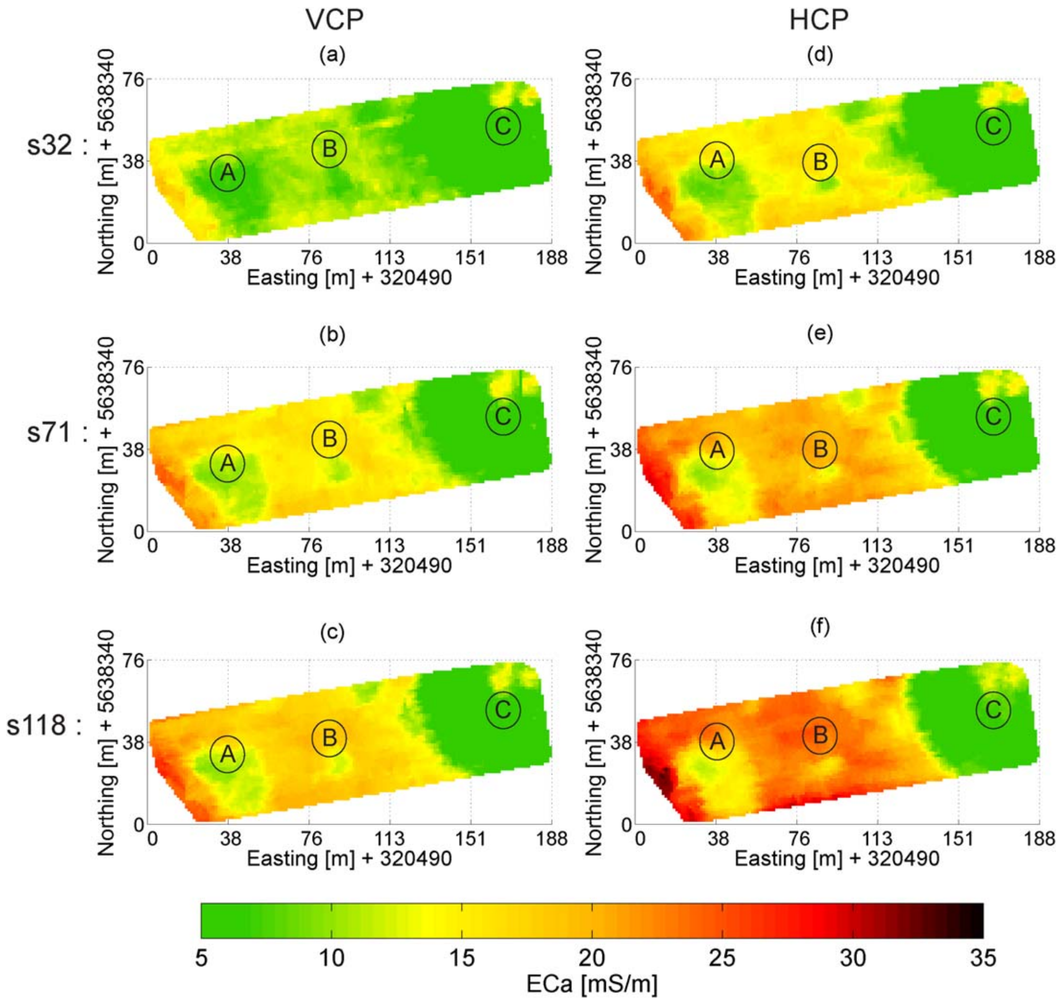

Figure 8. Calibrated ECa maps, histogram filtered and regridded, for VCP and HCP coil configuration for (a and d) s = 0.32 m, (b and e) s = 0.71 m, and (c and f) s = 1.18 m.

regularization used in the ERT inversion that smears the interfaces between adjacent structures, whereas the EMI inversion returns sharp layer boundaries. On the other hand, the EMI instrument has an accuracy of 4% and additional errors can occur due to the linear interpolation of deleted measurement positions.

4.2. Calibration and Quasi-3-D Inversion of the Large-Scale EMI Data

The obtained calibration parameters as shown in Figure 7 for the six coil configurations were applied to the processed and regridded large-scale EMI data. The resulting calibrated ECa maps are shown in Figures 8a–8c for the VCP mode and in Figures 8d–8f for HCP mode. For all EMI configurations, low ECa values around 5 mS/m were observed in the east indicating a relative homogeneous area. Beyond a sharp ECa boundary heading south-north, higher ECa values were observed in the western part of the test site. This is consistent with the grain size distribution shown in Figure 4, where finer material was present in the western part and coarse material was present in the eastern part. In addition to these main patterns, three smaller zones of contrasting ECa values can be distinguished.

Low-conductivity zone A has low ECa values for all coil configurations, which seems to coincide with a lower amount of clay shown in Figure 4d. Low-conductivity zone B does not coincide with any change in the sampled grain size distribution shown in Figure 4, and does not seem to extend as deep as zone A because the deepest sensing HCP coils show larger ECa values than the other coil configurations with shallower sensing depths. High-conductivity zone C seems to coincide with higher clay and silt contents shown in Figures 4c and 4d. Although the measured EMI data are consistent with the soil textural information, it is

© 2014. American Geophysical Union. All Rights Reserved.

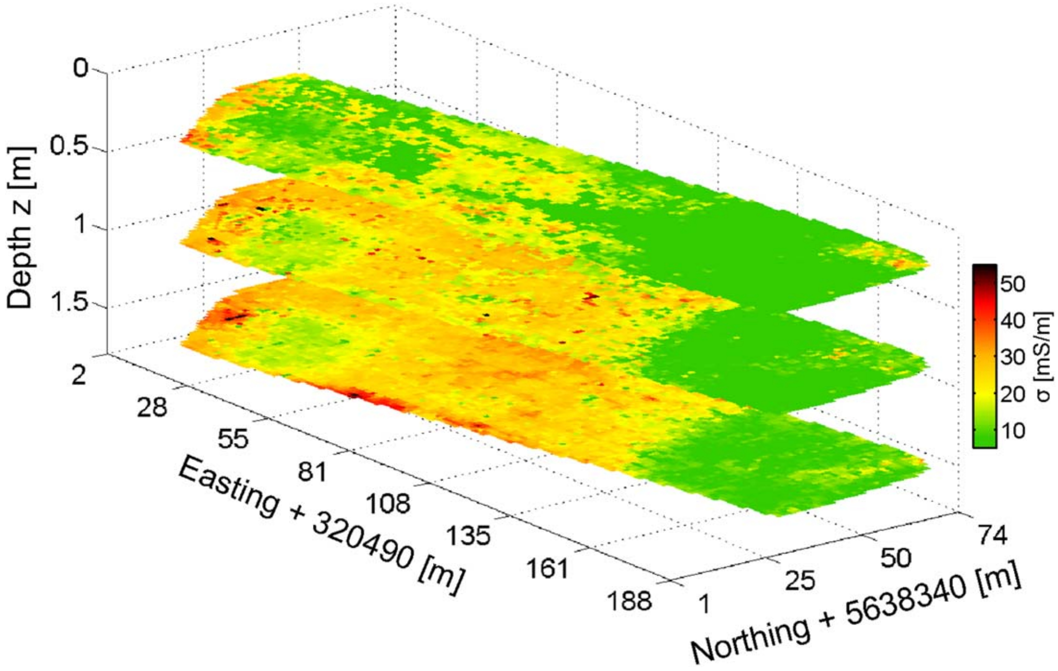

Figure 9. Horizontal depth slices at 0.25 m (ploughing zone), 0.55 m, and 1.55 m intersecting the main structures.

important to note that the grain size distribution shown in Figure 4 were obtained for the upper 30 cm on a 10 by 10 m coarse sampling grid, whereas the ECa values have been measured and resampled on a higher resolution grid such that high-resolution information was obtained.

At each grid node, the six quantitative ECa values were inverted for a three-layer 1-D electrical conductivity model. The results were stitched together to obtain a quasi 3-D three-layer model of the electrical conductivity distribution of the subsurface. Figure 9 shows horizontal slices through the obtained model at three different depth levels (0.25, 0.55, and 1.55 m).

A video of vertical depth slices through the three-dimensional electrical conductivity volume of the Selhausen test site can be watched at the IBG-3 homepage (http://www.fz-juelich.de/ibg/ibg-3/EN/Research/Research%20Topics/Hydrogeophysical%20Imaging%20and%20Characterisation/_node.html)

Figure 10 shows two vertical cross sections through the quasi 3-D electrical conductivity volume in the center plot, where the ploughed layer of about 30 cm thickness can be clearly identified. As already indicated in the calibrated ECa maps, patch A clearly extends to larger depths than patch B. Figure 10 also presents a comparison between the inverted EMI data and the two independent 120 m long ERT transects measured in 2009 and 2010 in bottom and top figures, respectively. Overall, the main electrical conductivity structures were remarkably similar. The bottom figure clearly shows the patches A and B and the three-layer area in the west. In the top figure, the noticeable transition of the homogeneous to a two-layer medium at about 120 m was found by the three-layer SCE inversion.

We conclude that the main structural patterns in the EMI and ERT data match well and are likely related to variations in soil texture. Remaining small-scale differences are to be expected because the ERT and EMI measurements in Figure 10 were performed at different dates with different weather conditions. From 1 until 27 May 2009, in total 43 mm rain were observed, while the sum of precipitation from 1 until 20 October 2010 was up to 35 mm. In June 2012, it rained 75 mm until the 28th. Hence, the soil was most probably drier in 2009 and 2010 than in 2012. However, in 2009 and 2010 about 5 and 8 mm precipitation were totally observed 5 days before the data acquisition, while no rain occurred within the 5 days before for the 2012 survey. Since the soil water content contributes to the EMI signal, we assume that remaining differences in electrical conductivity values might be caused by differences in the soil states, indicating that in future studies, repeated large-scale EMI measurements during dry and wet soil conditions can be used to identify hydrologically more active areas within the 3-D volume.

© 2014. American Geophysical Union. All Rights Reserved.

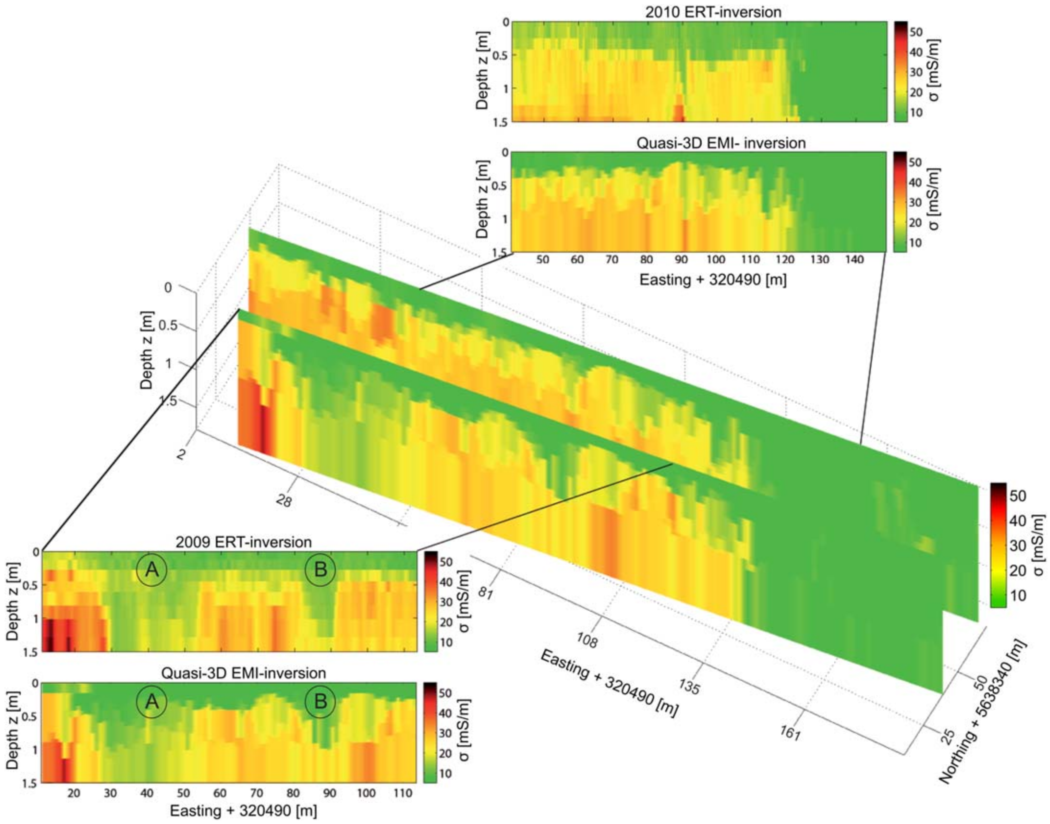

Figure 10. Quasi 3-D inversion slices in the middle and close-ups validated with (bottom left) the 2009 transect and (top right) the 2010 transect.

5. Conclusions and Outlook

Multiconfiguration EMI measurements can be performed quickly for efficient characterization of large-scale spatial variations in the subsurface electrical properties. To extract vertical changes, the measured ECa values for several EMI coil configurations with different sensing depths need to be filtered and subsequently calibrated with ERT to remove data shifts, e.g., due to the presence of the operator and/or acquisition setup. In this paper, a novel quasi 3-D large-scale inversion algorithm for calibrated multiconfiguration electromagnetic induction data measured in 2012 was developed that returns three-layer models at each grid location assuming a horizontally layered earth. The obtained 1-D models were stitched together to image a 3-D subsurface to reveal lateral and vertical structural electrical conductivity patterns, which are related to the observed variations in soil texture and soil water content. ERT transects measured in 2009 and 2010 reveal similar electrical conductivity structures at the same locations, whereas small changes in absolute electrical conductivity values are probably due to the different soil states at different dates. To obtain reliable inversion results quantitative ECa values are required for which a 30 m calibration line (collocated ERT and EMI measurements) is recorded. This transect ideally covers the lateral variations of the soil apparent electrical conductivity distribution as observed in the field's data. Linear regressions between measured and predicted ECa obtain coil specific calibration parameters that are applied to the large-scale data. Due to the time stability of the used CMD-MiniExplorer and the similar ECa range of transect and field data, this short calibration line could be used to obtain quantitative ECa values over a much larger area.

The presented results show the potential and reliability of large-scale EMI measurements and inversions with the advantage that subsurface models can be obtained in relatively short times. In principle, the flexible and mobile measurements and efficient inversions can also be performed for larger coil offset EMI systems with a deeper sensing depth, which opens up an even broader range of applications. However, the

© 2014. American Geophysical Union. All Rights Reserved.

performance in highly resistive areas needs further investigation. In future tasks, repeated large-scale EMI measurements and inversions are performed for different soil states such that the electrical conductivity changes and hence soil water dynamics within certain layers can be observed. Conclusively, the presented approach turns the EMI usage from a simple proxy indicator toward a more valuable tool that quantitatively characterizes the ground such that a wide range of catchment scale applications that lack in vertical and/or lateral resolution can benefit from the provided information.

Acknowledgments
We thank Daniel Altdorff and Jutta Bikowski for their support while preparing the paper. We thank the three anonymous reviewers and the Associate Editor Andrew Binley for their comments that improved the paper. We also acknowledge support by SFB/TR32 "Pattern in Soil-Vegetation-Atmosphere Systems: Monitoring, Modelling, and Data Assimilation" funded by the Deutsche Forschungsgemeinschaft (DFG), "TERestrial Environmental Observations" (TERENO), Centre for High-Performance Scientific Computing in Terrestrial Systems (TerrSys), Advanced Remote Sensing—Ground-Truth Demo and Test Facilities (ACROSS), and the Jülich supercomputer center (JSC).

References

Abdu, H., D. A. Robinson, M. Seyfried, and S. B. Jones (2008), Geophysical imaging of watershed subsurface patterns and prediction of soil texture and water holding capacity, *Water Resour. Res.*, *44*, W00D18, doi:10.1029/2008WR007043.

Anderson, W. (1979), Numerical integration of related Hankel transforms of orders 0 and 1 by adaptive digital filtering, *Geophysics*, *44*(7), 1287–1305.

Auken, E., A. V. Christiansen, B. H. Jacobsen, N. Foged, and K. I. Sørensen (2005), Piecewise 1D laterally constrained inversion of resistivity data, *Geophys. Prospect.*, *53*(4), 497–506.

Beamish, D. (2011), Low induction number, ground conductivity meters: A correction procedure in the absence of magnetic effects, *J. Appl. Geophys.*, *75*(2), 244–253.

Bogena, H. R., M. Herbst, J. A. Huisman, U. Rosenbaum, A. Weuthen, and H. Vereecken (2010), Potential of wireless sensor networks for measuring soil water content variability, *Vadose Zone J.*, *9*(4), 1002–1013.

Brosten, T. R., F. D. Day-Lewis, G. M. Schultz, G. P. Curtis, and J. W. Lane Jr. (2011), Inversion of multi-frequency electromagnetic induction data for 3D characterization of hydraulic conductivity, *J. Appl. Geophys.*, *73*(4), 323–335.

Busch, S., J. van der Kruk, and H. Vereecken (2014), Improved characterization of fine texture soils using on-ground GPR full-waveform inversion, *IEEE Trans. Geosci. Remote Sens.*, *52*(7), 3947–3958, doi:10.1109/TGRS.2013.2278297.

Callegary, J. B., T. P. A. Ferre, and R. W. Groom (2012), Three-dimensional sensitivity distribution and sample volume of low-induction-number electromagnetic-induction instruments, *Soil Sci. Soc. Am. J.*, *76*(1), 85–91.

Corwin, D. L., and S. M. Lesch (2005), Apparent soil electrical conductivity measurements in agriculture, *Comput. Electron. Agric.*, *46*(1–3), 11–43.

Duan, Q. Y., S. Sorooshian, and V. K. Gupta (1992), Effective and efficient global optimization for conceptual rainfall-runoff models, *Water Resour. Res.*, *28*(4), 1015–1031.

Duan, Q. Y., V. K. Gupta, and S. Sorooshian (1993), Suffled complex evolution approach for effective and efficient global minimization, *J. Opt. Theory Appl.*, *76*(3), 501–521.

Gebbers, R., E. Lueck, M. Dabas, and H. Domsch (2009), Comparison of instruments for geoelectrical soil mapping at the field scale, *Near Surf. Geophys.*, *7*(3), 179–190.

GF-Instruments (2011), *CMD Electromagnetic Conductivity Meter User Manual V. 1.5*, GF Instruments s.r.o. Geophysical Equipment and Services.

Hardie, M., and R. Doyle (2012), Measuring soil salinity, in *T Plant Salt Tolerance*, pp. 415–425, Springer, New York.

Kaufman, A. A., and G. V. Keller (1983), *Frequency and Transient Soundings*, vol. *21*, 685 pp., Elsevier Sci., Amsterdam.

Keller, G. V., and F. C. Frischknecht (1966), *Electrical Methods of Geophysical Prospecting, Int. Ser. Monogr. Electromagn. Waves*, vol. *10*, Pergamon, Oxford, N. Y.

Kerr, Y. H., P. Waldteufel, J. P. Wigneron, J. M. Martinuzzi, J. Font, and M. Berger (2001), Soil moisture retrieval from space: The Soil Moisture and Ocean Salinity (SMOS) mission, *IEEE Trans. Geosci. Remote Sens.*, *39*(8), 1729–1735.

Kirsch, R. (2009), *Groundwater Geophysics*, 2nd ed., 548 pp., Springer, Berlin.

Lavoué, F., J. van der Kruk, J. Rings, F. Andre, D. Moghadas, J. A. Huisman, S. Lambot, L. Weihermüller, J. Vanderborght, and H. Vereecken (2010), Electromagnetic induction calibration using apparent electrical conductivity modelling based on electrical resistivity tomography, *Near Surf. Geophys.*, *8*(6), 553–561.

Loke, M. H., I. Acworth, and T. Dahlin, (2003), A comparison of smooth and blocky inversion methods in 2D electrical imaging surveys, *Explor. Geophys.*, *34*(3), 182–187, doi: 10.1071/EG03182.

Mboh, C. M., J. A. Huisman, and H. Vereecken (2011), Feasibility of sequential and coupled inversion of time domain reflectometry data to infer soil hydraulic parameters under falling head infiltration, *Soil Sci. Soc. Am. J.*, *75*(3), 775–786.

McNeill, J. D. (1980), Electromagnetic terrain conductivity measurement at low induction numbers, *Tech. Note TN-6*, Geonics Ltd., Mississauga, Ont., Canada.

Mester, A., J. van der Kruk, E. Zimmermann, and H. Vereecken (2011), Quantitative two-layer conductivity inversion of multi-configuration electromagnetic induction measurements, *Vadose Zone J.*, *10*(4), 1319–1330.

Minsley, B. J., B. D. Smith, R. Hammack, J. I. Sams, and G. Veloski (2012), Calibration and filtering strategies for frequency domain electromagnetic data, *J. Appl. Geophys.*, *80*, 56–66.

Moghadas, D., F. Andre, J. H. Bradford, J. van der Kruk, H. Vereecken, and S. Lambot (2012), Electromagnetic induction antenna modelling using a linear system of complex antenna transfer functions, *Near Surf. Geophys.*, *10*(3), 237–247.

Montzka, C., H. Moradkhani, L. Weihermüller, H.-J. H. Franssen, M. Canty, and H. Vereecken (2011), Hydraulic parameter estimation by remotely-sensed top soil moisture observations with the particle filter, *J. Hydrol.*, *399*(3–4), 410–421.

Nüsch, A. K., P. Dietrich, U. Werban, and T. Behrens (2010), Acquisition and reliability of geophysical data in soil science, paper presented at 19th World Congress of Soil Science, Solutions for a Changing World, iSOIL Project, Brisbane, Australia.

Robinson, D. A., S. B. Jones, J. M. Wraith, D. Or, and S. P. Friedman (2003), A review of advances in dielectric and electrical conductivity measurement in soils using time domain reflectometry, *Vadose Zone J.*, *2*(4), 444–475.

Robinson, D. A., C. S. Campbell, J. W. Hopmans, B. K. Hornbuckle, S. B. Jones, R. Knight, F. Ogden, J. Selker, and O. Wendroth (2008), Soil moisture measurement for ecological and hydrological watershed-scale observatories: A review, *Vadose Zone J.*, *7*(1), 358–389.

Robinson, D. A., I. Lebron, B. Kocar, K. Phan, M. Sampson, N. Crook, and S. Fendorf (2009), Time-lapse geophysical imaging of soil moisture dynamics in tropical deltaic soils: An aid to interpreting hydrological and geochemical processes, *Water Resour. Res.*, *45*, W00D32, doi: 10.1029/2008WR006984.

Robinson, D. A., H. Abdu, I. Lebron, and S. B. Jones (2012), Imaging of hill-slope soil moisture wetting patterns in a semi-arid oak savanna catchment using time-lapse electromagnetic induction, *J. Hydrol.*, *416–417*, 39–49.

© 2014. American Geophysical Union. All Rights Reserved.

Rosenbaum, U., H. R. Bogena, M. Herbst, J. A. Huisman, T. J. Peterson, A. Weuthen, A. W. Western, and H. Vereecken (2012), Seasonal and event dynamics of spatial soil moisture patterns at the small catchment scale, *Water Resour. Res.*, *48*, W10544, doi:10.1029/2011WR011518.

Saey, T., P. De Smedt, M. M. Islam, E. Meerschman, E. V. De Vijver, A. Lehouck, and M. Van Meirvenne (2012), Depth slicing of multi-receiver EMI measurements to enhance the delineation of contrasting subsoil features, *Geoderma*, *189*, 514–521.

Saey, T., P. De Smedt, W. De Clercq, E. Meerschman, M. M. Islam, and M. Van Meirvenne (2013), Identifying soil patterns at different spatial scales with a multi-receiver emi sensor, *Soil Sci. Soc. Am. J.*, *77*(2), 382–390.

Santos, F. A. M., J. Triantafilis, K. E. Bruzgulis, and J. A. E. Roe (2010), Inversion of multiconfiguration electromagnetic (DUALEM-421) profiling data using a one-dimensional laterally constrained algorithm, *Vadose Zone J.*, *9*(1), 117–125.

Sheets, K. R., and J. M. H. Hendrickx (1995), Noninvasive soil water content measurement using electromagnetic induction, *Water Resour. Res.*, *31*(10), 2401–2409.

Slob, E., and J. Fokkema (2002), Coupling effects of two electric dipoles on an interface, *Radio Sci.*, *37*(5), 1073, doi:10.1029/2001RS002529.

Sørense, K. I., and E. Auken (2004), SkyTEM—A new high-resolution helicopter transient electromagnetic system, *Explor. Geophys.*, *35*(3), 194–202.

Sudduth, K. A., S. T. Drummond, and N. R. Kitchen (2001), Accuracy issues in electromagnetic induction sensing of soil electrical conductivity for precision agriculture, *Comput. Electron. Agric.*, *31*(3), 239–264.

Sudduth, K. A., et al. (2005), Relating apparent electrical conductivity to soil properties across the north-central USA, *Comput. Electron. Agric.*, *46*(1–3), 263–283.

Sudduth, K. A., D. B. Myers, N. R. Kitchen, and S. T. Drummond (2013), Modeling soil electrical conductivity-depth relationships with data from proximal and penetrating ECa sensors, *Geoderma*, *199*, 12–21.

Triantafilis, J., G. M. Laslett, and A. B. McBratney (2000), Calibrating an electromagnetic induction instrument to measure salinity in soil under irrigated cotton, *Soil Sci. Soc. Am. J.*, *64*(3), 1009–1017.

Vereecken, H., J. A. Huisman, H. Bogena, J. Vanderborght, J. A. Vrugt, and J. W. Hopmans (2008), On the value of soil moisture measurements in vadose zone hydrology: A review, *Water Resour. Res.*, *44*, W00D06, doi:10.1029/2008WR006829.

Vrugt, J. A., H. V. Gupta, W. Bouten, and S. Sorooshian (2003), A Shuffled Complex Evolution Metropolis algorithm for optimization and uncertainty assessment of hydrologic model parameters, *Water Resour. Res.*, *39*(8), 1201, doi:10.1029/2002WR001642.

Wait, J. R. (1982), *Geo-electromagnetism*, vol. *37*, pp. 288–289, Academic, New York.

Ward, S., and G. Hohmann (1988), Electromagnetic theory for geophysical applications, in *Electromagnetic Methods in Applied Geophysics*, pp. 130–311, Society of Exploration Geophysicists, Tulsa, Okla.

Weihermüller, L., J. A. Huisman, S. Lambot, M. Herbst, and H. Vereecken (2007), Mapping the spatial variation of soil water content at the field scale with different ground penetrating radar techniques, *J. Hydrol.*, *340*(3–4), 205–216.

© 2014. American Geophysical Union. All Rights Reserved.